

## Electronic Supplementary Information

### Thickness-Dependent Bandgap and Electrical Properties of GeP Nanosheets

Doyeon Kim,<sup>a</sup> Kidong Park,<sup>a</sup> Fazel Shojaei,<sup>b,c,d</sup> Tekalign Terfa Debela,<sup>e</sup> Ik Seon Kwon,<sup>a</sup> In  
Hye Kwak,<sup>a</sup> Jaemin Seo,<sup>a</sup> Jae Pyoung Ahn,<sup>f</sup> Jeunghee Park,<sup>\*,a</sup> and Hong Seok Kang<sup>\*,g</sup>

<sup>a</sup> Department of Chemistry, Korea University, Sejong 339-700, Republic of Korea; <sup>b</sup>  
Department of Chemistry and Bioactive Material Science, Jeonbuk National University,  
Chonju, Republic of Korea; <sup>c</sup> School of Nanoscience, institute for Research in Fundamental  
Sciences (IPM), P.O.BOX: 19395-5531, Tehran, Iran; <sup>d</sup> Department of Chemistry, faculty of  
Science, Shahid Chamran University, Ahvaz, Iran; <sup>e</sup> Institute for Application of Advanced  
Materials, Jeonju University, Chonju, Chonbuk 55069, Republic of Korea; <sup>f</sup> Korea Advanced  
Analysis Center, Korea Institute of Science and Technology, Seoul 136-791, Republic of  
Korea; <sup>g</sup> Department of Nano and Advanced Materials, College of Engineering, Jeonju  
University, Chonju, Chonbuk 560-759, Republic of Korea.

\*[parkjh@korea.ac.kr](mailto:parkjh@korea.ac.kr); [hsk@jj.ac.kr](mailto:hsk@jj.ac.kr)

## Contents

### Experimental Section

**Figure S1.** XRD patterns of GeP.

**Figure S2.** Raman spectrum of GeP nanosheets.

**Figure S3.** SEM image of exfoliated GeP nanosheets.

**Figure S4.** Band structures of GeP tetralayer (4L) and bulk GeP.

**Figure S5.** I-V curves of FET device fabricated using GeP nanosheets.

**Table S1.** Summary of thickness-dependent FET characteristics.

**Figure S6.** Anisotropic I-V curves of GeP nanosheets.

**Table S2.** Summary of anisotropic FET characteristics.

**Figure S7.** Temperature-dependent FET characteristics.

**Figure S8.** Temperature-dependent conductivity of GeP nanosheets.

**Figure S9.** H<sub>2</sub>/O<sub>2</sub> gas evolution data of PEC cells.

**Figure S10.** (a) Solar energy conversion efficiency curve and (b) incident-photon-to-current-conversion efficiency data.

**Table S3.** PEC cell parameters.

**Figure S11.** XPS and TEM data for the Si-GeP photoanodes after 1 h PEC water splitting.

**Table S4.** Comparison of PEC performance (in pH 0) of Si photoanode in the literatures.

**Figure S12.** Nyquist plots of GeP nanosheets, Si NWs, and Si-GeP NWs.

**Table S5.** Fitting parameters of Nyquist plots.

**Figure S13.** Mott–Schottky plots of Si and Si-GeP NWs.

**Figure S14.** Band alignment of GeP and Si.

### References

## Experimental Section

### (1) Characterization

The structure and composition of the products were analyzed by scanning electron microscopy (SEM, Hitachi S-4700), field-emission transmission electron microscopy (FETEM, FEI TECNAI G<sup>2</sup>, 200 kV), high-voltage TEM (Jeol JEM ARM 1300S, 1.25 MV), and energy-dispersive X-ray fluorescence spectroscopy (EDX). Fast Fourier transform (FFT) images were generated by inversion of the TEM images using Digital Micrograph GMS1.4 software (Gatan). A tilt holder (Dual Orientation Tomography Holder 927, Gatan) was used for the TEM measurements.

High-resolution XRD patterns were obtained using the 9B and 3D beamlines of the Pohang Light Source (PLS) with monochromatic radiation. X-ray photoelectron spectroscopy (XPS) measurements were performed using the 8A1 beam line of the PLS. A UV-Vis-NIR spectrometer (Agilent Cary 6000) was used to measure the UV-visible absorption of samples. The Raman spectra of individual GeP samples were measured with a homemade micro-Raman system (using 514 nm Ar ion laser) and a commercial micro-Raman spectrometer (HORIBA ARAMIS IR2, 532 nm diode laser). The spectral resolution was about 1 cm<sup>-1</sup>. A laser power below 0.5 mW was used to avoid heating effects.

### (2) Field-effect transistors

Photolithography was used to deposit Ti (20 nm)/Au (80 nm) electrodes on a silicon substrate with a 300-nm-thick thermally grown silicon oxide layer, by sputtering using a patterned mask. The highly B-doped Si (*p*-Si) substrate (resistivity < 0.005 Ω·cm) was used for a back gate. The GeP nanosheets were transferred by mechanical exfoliation using a tape (Nitto Denko

Corp.) onto a patterned Si substrate. The samples were then coated with a layer of poly(methyl methacrylate) (PMMA, A4, Microchem.) and copolymer (EL11, Microchem.), and the electrode patterns were created in an electron-beam lithography process. After developing, the samples were loaded in an electron beam evaporator, and 20 nm of Ti was deposited, followed by 100 nm of Au. After the lift-off process, the samples were then annealed again in vacuum at 200 °C for 2 h to remove the fabrication residues. The electrical transport properties were measured in a commercial probe station (WWIT Co. VPX-10) with the Au probe tip that is connected to a parametric test equipment (Agilent E5270A). The temperature was varied from 80 K to 320 K. The pressure of the probe chamber was maintained at  $10^{-3}$  Torr.

### (3) Water-splitting PEC cells

Si NWs were fabricated by Ag-assisted chemical etching. *n*-Type (100) Si wafers (area = 2 cm<sup>2</sup>) lightly doped with phosphor ( $R = 1\text{--}10 \Omega \text{ cm}$ ) were electrochemically etched using a mixed solution of 4.8 M HF/0.005 M AgNO<sub>3</sub>/0.4 M H<sub>2</sub>O<sub>2</sub>. After 5 min etching, the Si wafers were washed repeatedly with water and immersed in 30% HNO<sub>3</sub> solution to dissolve the Ag nanoparticles. The etched Si wafers were then washed with 5% HF solution to remove the oxide layer and cleaned with distilled water. The GeP nanosheets were deposited on a piece of Si NW substrate (area = 1 × 1 cm<sup>2</sup>) by drop-casting or spin coating the NMP solution, immediately followed by annealing at 200 °C for 2 h in vacuum to remove the solvent. This process was repeated a few times. The Si or Si-GeP NW electrode was connected to a Cu wire using an In–Ga alloy (99.99%, Sigma-Aldrich) and silver paste, and the Cu wire was covered with epoxy glue.

The PEC cell experiments were carried out in a three-electrode cell using an electrochemical

analyzer (Ivium CompactStat). Ag/AgCl electrode was used as reference electrode, and a Pt wire as the counter electrode. The potentials were referenced to the reversible hydrogen electrode (RHE) using standard RHE calibration. Since the electrolyte was 0.1 M Na<sub>2</sub>SO<sub>4</sub>/0.25 M NaOH at pH 13, we have  $E$  (vs. RHE) =  $E$  (vs. Ag/AgCl) +  $E_{\text{Ag/AgCl}}$  + 0.0592 pH =  $E$  (Ag/AgCl) + 0.967 V, whereas  $E_{\text{Ag/AgCl}} = 0.197$  V. A 450 W Xe lamp was used with an AM1.5G filter. The light intensity (100 mW/cm<sup>2</sup>) was calibrated using a Si solar cell (Abet Technologies, Model 15150 Reference Cell).

The hydrogen (H<sub>2</sub>) and oxygen (O<sub>2</sub>) gas evolution by the PEC water splitting was conducted in an airtight reactor and monitored using gas chromatography (GC, Young Lin ACME 6100). A pulsed discharge detector (VICI, Valco Instruments Co., Inc.) and a GC column (SUPELCO Molecular Sieve 13X) were used. The quantities of H<sub>2</sub> and O<sub>2</sub> were calibrated using standard H<sub>2</sub>/He and O<sub>2</sub>/He mixtures.

Electrochemical impedance spectroscopy measurements were performed by applying an AC voltage of 10 mV in the frequency range of 100 kHz (or 1 MHz)–0.1 Hz at 1.23 V (vs. RHE). The working electrodes were prepared by drop-casting the sample (0.2 mg dispersed in Nafion using isopropyl alcohol) over a glassy carbon (GC) electrode (area = 0.1963 cm<sup>2</sup>, Pine Instruments, Model No. AFE5T050GC). The Mott-Schottky curves were measured by sweeping the potential with an AC amplitude of 10 mV or 20 mV.

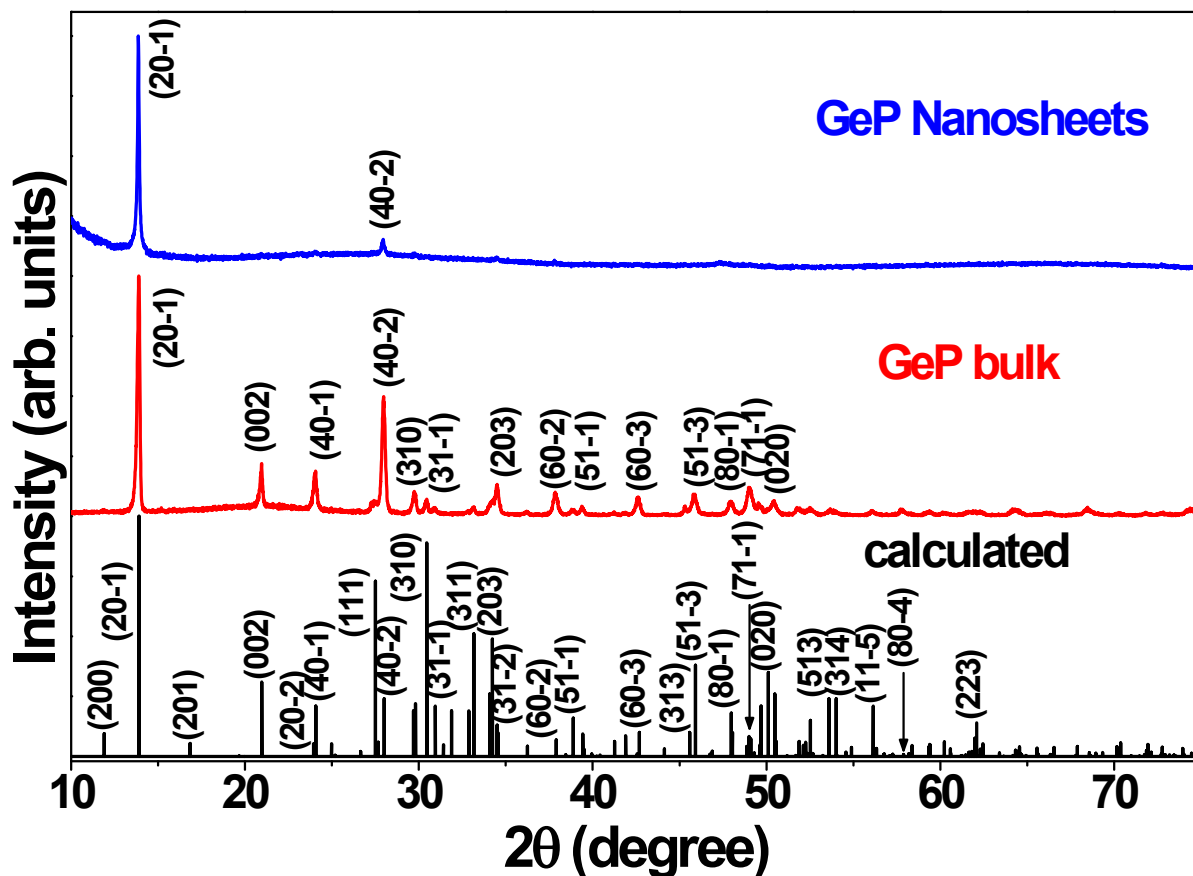


**Figure S1.** XRD patterns of GeP bulk and nanosheets (synthesized using the exfoliation in NMP and filtered on the AAO membrane). The reference peaks are generated for monoclinic phase GeP ( $a = 15.140 \text{ \AA}$ ,  $b = 3.638 \text{ \AA}$ ,  $c = 9.190 \text{ \AA}$ ,  $\beta = 101.1^\circ$ ).<sup>S1</sup> VESTA program (<http://jp-minerals.org/vesta/en/>) was used to generate the simulated XRD pattern. All peak position is well matched with that of the reference. The bulk crystal shows the strong peaks originating from the layer axis [20], (-201) and (-402). The GeP nanosheet show only those peaks originating from the layer axis [20].

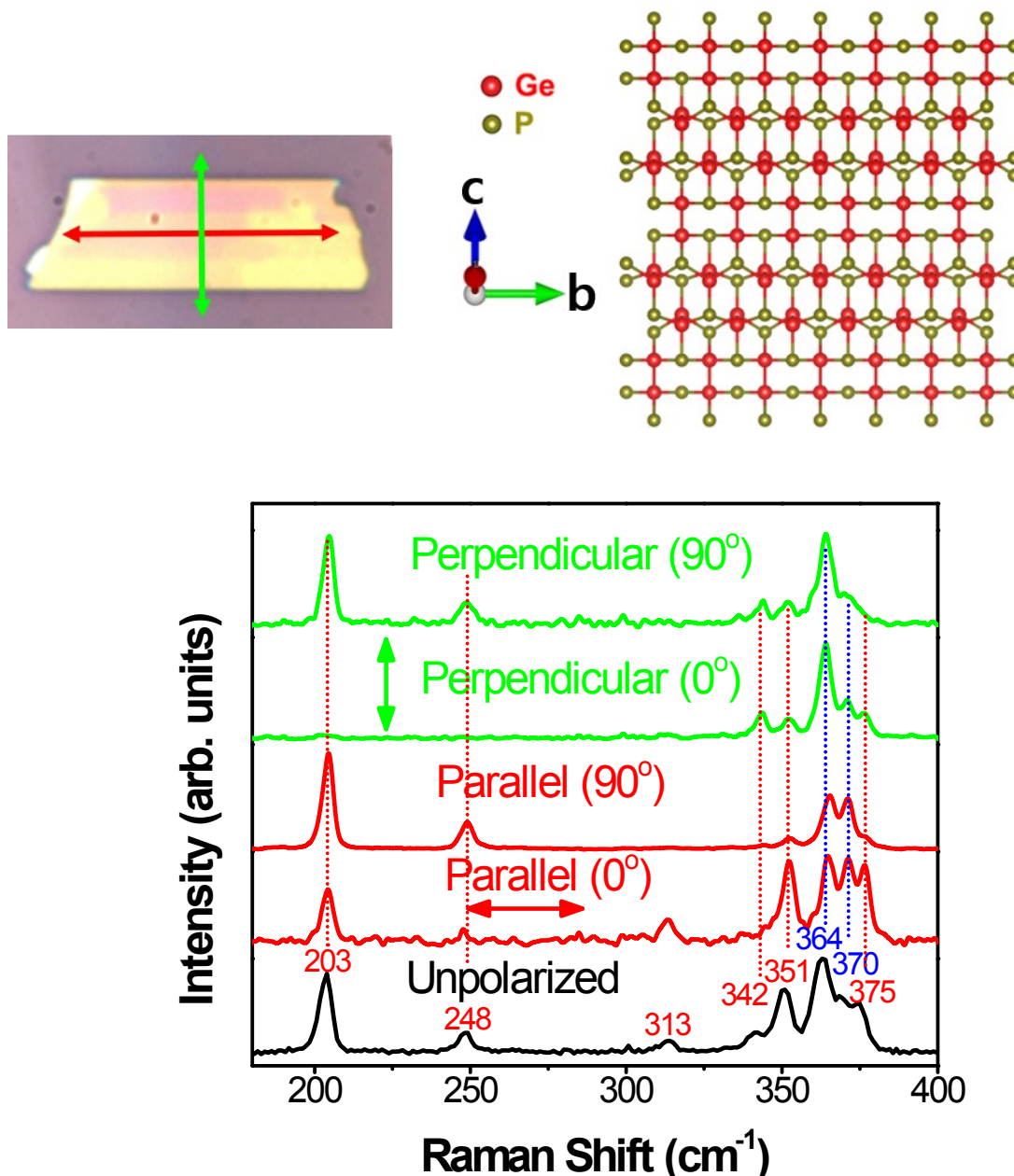


**Figure S2.** Raman spectra of GeP nanosheets (thickness = 30 nm), measured at angle of  $0^\circ$  (and  $90^\circ$ ) under unpolarized, parallel-polarized, and perpendicular-polarized configurations relative to the long axis ( $[010]$ ). Excitation at the wavelength of 514 nm was provided from Ar-ion laser. The optical image of nanosheets and its corresponding molecular structure of basal plane at the  $[20]$  zone axis (monoclinic phase) are shown on the top.

The Raman scans were obtained using exciting polarized light that is parallel or perpendicular to the long axis. A linear polarizer was placed before the detector and the Raman signals were

collected at angles of  $0^\circ$  and  $90^\circ$  (degrees) under parallel and perpendicular configurations. Unpolarized Raman spectrum was also measured for reference. The peaks at  $203\text{ cm}^{-1}$  ( $A_g$  mode),  $248\text{ cm}^{-1}$  ( $A_g$  mode),  $313\text{ cm}^{-1}$  ( $A_g$  mode),  $342\text{ cm}^{-1}$  ( $B_g$  mode),  $351\text{ cm}^{-1}$  ( $A_g$  mode),  $364\text{ cm}^{-1}$  ( $B_g$  mode),  $370\text{ cm}^{-1}$  ( $B_g$  mode), and  $375\text{ cm}^{-1}$  ( $A_g$  mode) are observed. The intensity of Raman modes shows the polarization dependent behavior, which is consistent with the results reported by Li et al.<sup>S2</sup>

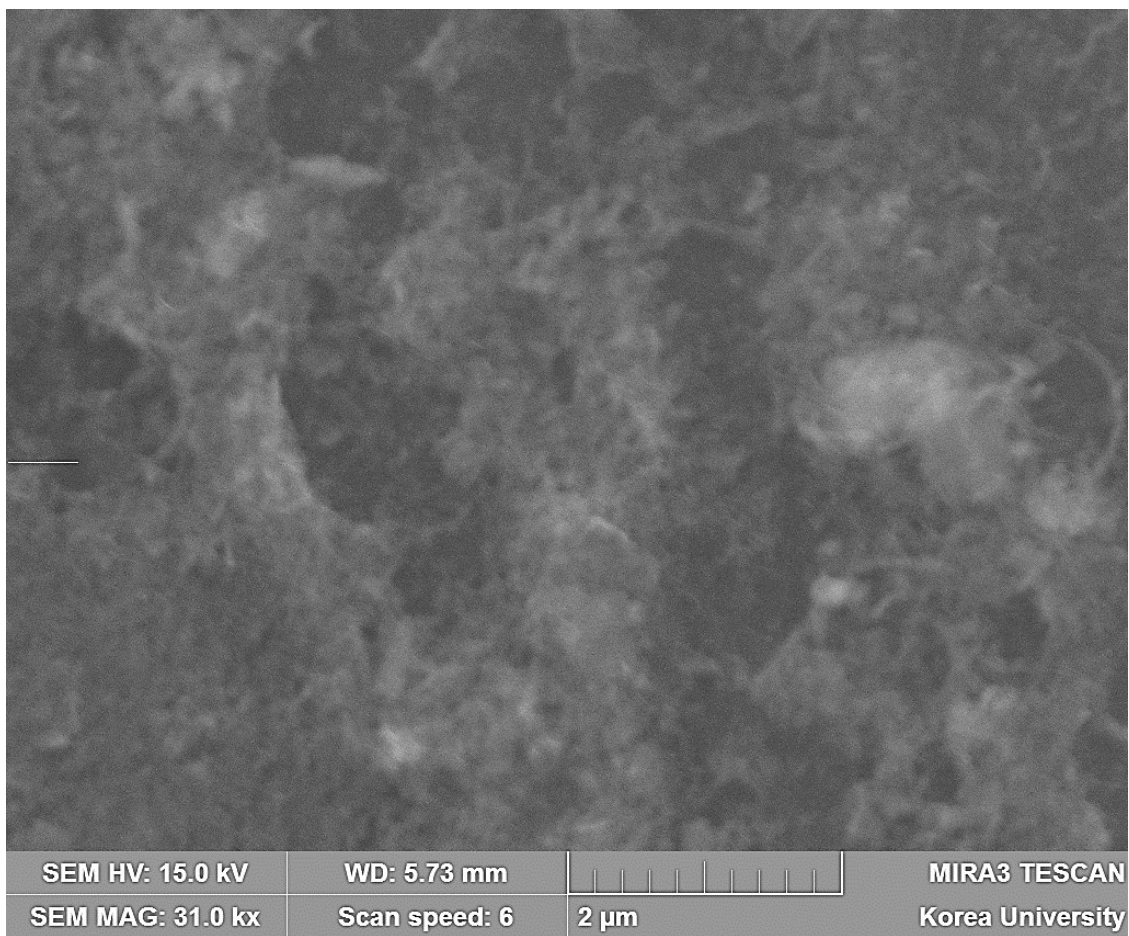


**Figure S3.** High-resolution SEM images for liquid-phase exfoliated GeP that deposited on the Si substrate, showing that the GeP crystal were effectively exfoliated into the thin nanosheets.

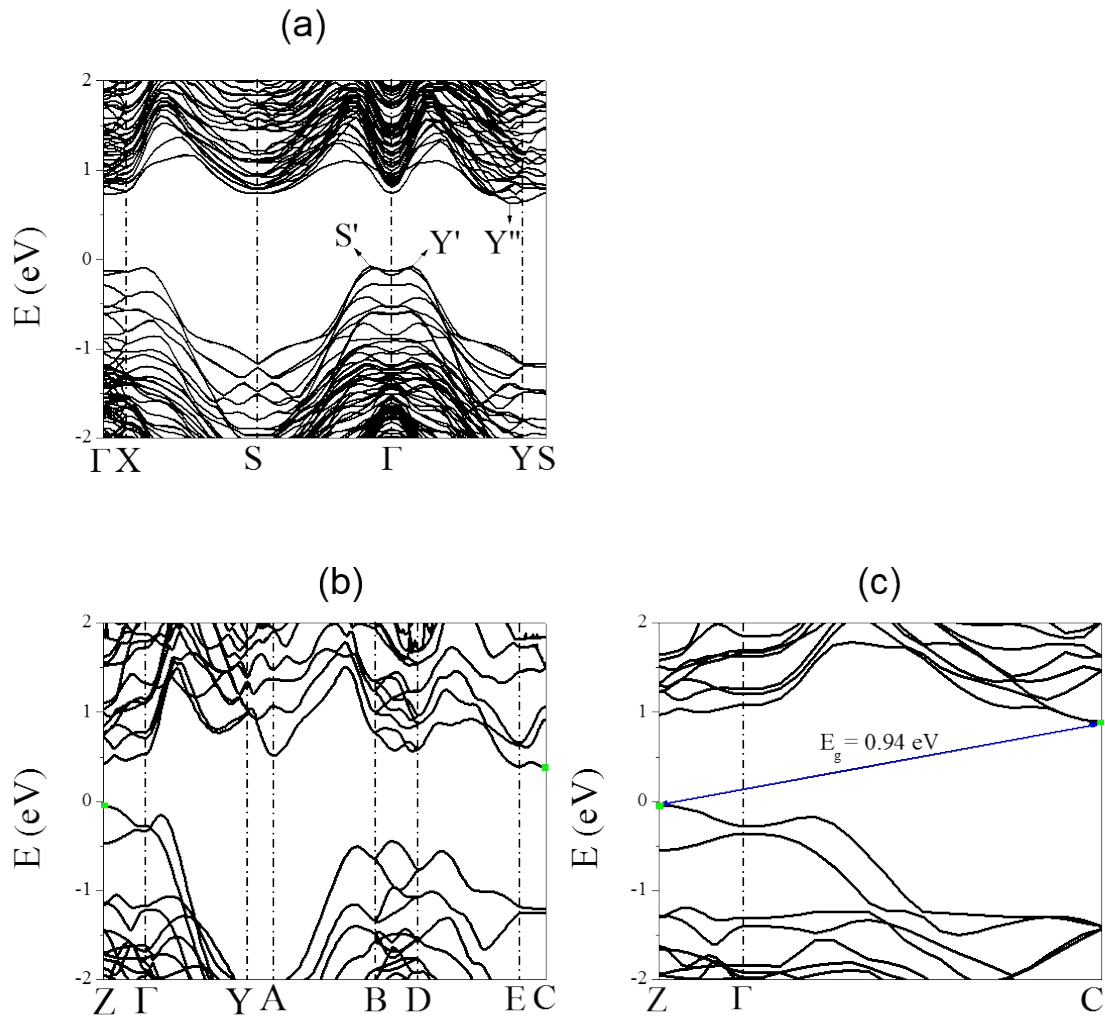
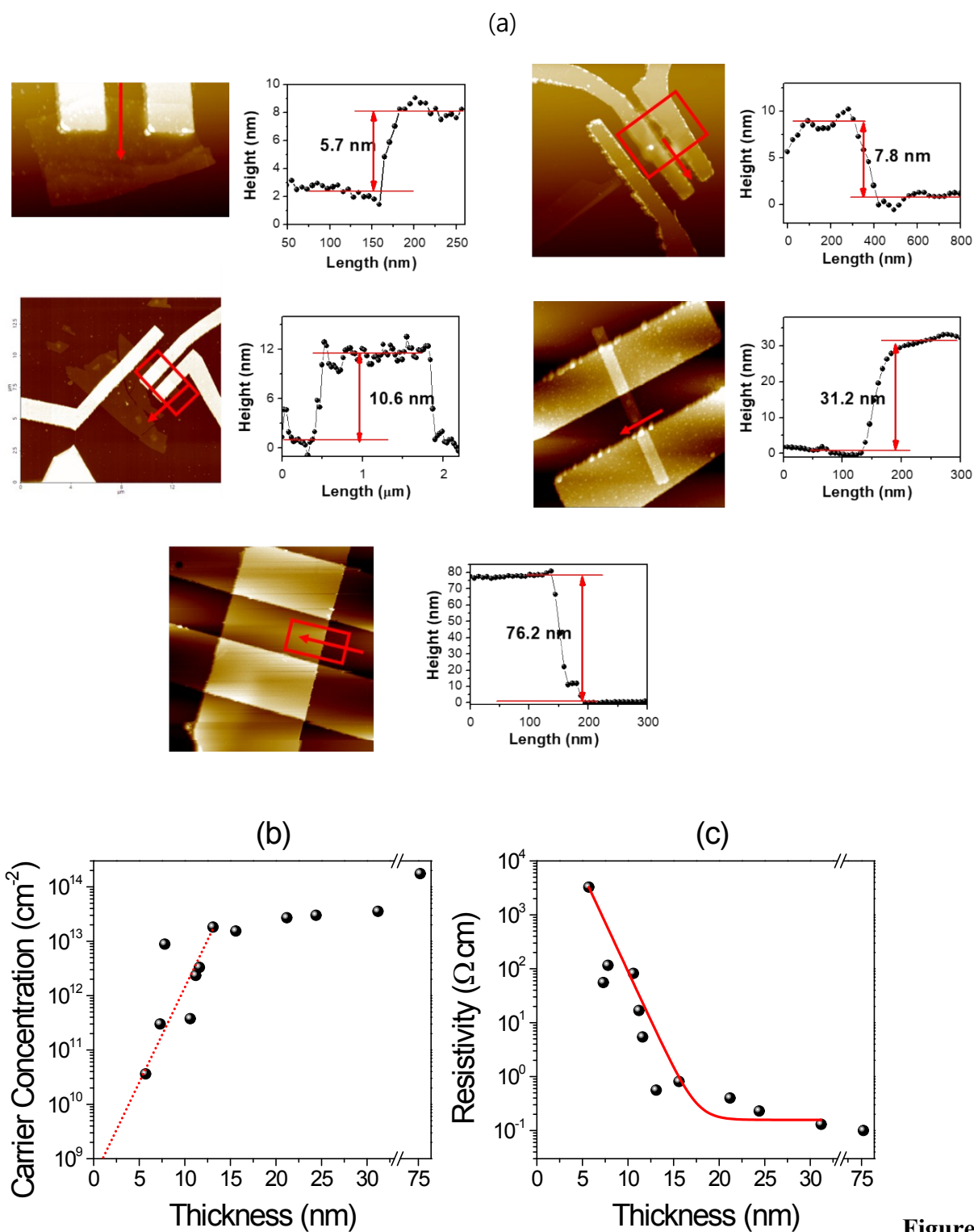


**Figure S4.** (a) The PBE-D3 band structure of GeP tetralayer (4L). (b) PBE-D3 and (c) HSE06 band structures of bulk GeP. The HSE06 calculations are done in selected  $k$ -paths, considering that the band gap corresponds to  $Z \rightarrow C$  transition.

The calculation of its HSE06 band structure in the full  $k$ -path is quite time-consuming. Therefore, PBE band structure is calculated first to show that its band edge positions are still located around the  $\Gamma$ -point in the same way as in 3L. Therefore, the HSE06 band structure is drawn in the limited path, i.e., in  $[\Gamma, Y]$ . The band gap calculated using HSE06 functionals is 0.94 eV, which is consistent with the experimental value (0.9 eV).



**S5.** (a) AFM images and high profiles for the electrodes of FET device (**Fig. 4**), showing the length and width of electrode as well as the thickness of GeP nanosheet: 5.7 nm, 7.8, 10.6,

31.2, and 76.2 nm. (b) 2D carrier concentration and (c) resistivity as a function of the thickness of GeP nanosheet.

(a) The photographs and AFM images of each electrode show the distance between the electrodes and the thickness of GeP nanosheets (5.7, 7.8, 10.6, 31.2, and 76.2 nm). The reproducible source-drain current ( $I_{SD}$ ) as a function of (back) gate voltage ( $V_G$ ) at 0.05-3.0 V of source-drain ( $V_{SD}$ ) was obtained for 11 field-effect transistor (FET) devices under ambient condition (298 K). The  $I_{SD}$  increases with increasingly negative  $V_G$ , indicating the characteristics of *p*-type semiconductor. From the linear region of the  $I_{SD}$ - $V_G$  curve (see the

linear fit line), the transconductance ( $g_m = \left| \frac{\partial I_{SD}}{\partial V_G} \right|$ ) can be obtained by extrapolation. The channel mobility,  $\mu$ , was estimated to be in a unit of  $\text{cm}^2 \text{V}^{-1} \text{s}^{-1}$  using the equation,

$$\mu = g_m \frac{L}{W} \frac{1}{V_{SD}} \frac{1}{C_G} = g_m \left( \frac{L}{W} \right) \left( \frac{1}{V_{SD}} \right) \left( \frac{d}{\varepsilon \varepsilon_0} \right),$$

where  $h$  is the thickness of  $\text{SiO}_2$  (300 nm),  $L$  is the channel length of electrode,  $W$  is the width of electrode (based on the value measured by AFM images),  $V_{SD}$  is the bias voltage between the source and drain, and the gate capacitance per unit area  $C_G$  is  $\frac{\varepsilon \varepsilon_0}{d}$  (where  $\varepsilon$  is the relative dielectric constant of  $\text{SiO}_2$  (3.9) and  $\varepsilon_0$  is the dielectric constant

of vacuum ( $= 8.85 \times 10^{-12} \text{ J}^{-1} \text{ C}^2 \text{ m}^{-1} = 8.85 \times 10^{-12} \text{ F m}^{-1}$ ). The  $\left( \frac{d}{\varepsilon \varepsilon_0} \right)$  is calculated as  $\frac{3 \times 10^{-7}}{3.4515 \times 10^{-11}} = 8.69 \times 10^3 \text{ J}^{-1} \text{ C}^2 \text{ m}^{-1}$ . The carrier concentration ( $n$ ) in 2D (in  $\text{cm}^{-2}$ ) is calculated

using the equation:  $n = \left( \frac{\sigma}{e\mu} \right)$ , where  $e$  is  $1.602 \times 10^{-19} \text{ C}$  and  $\sigma_{2D}$  is conductivity defined as

$$\left( \frac{I_{SD}}{V_{SD}} \right) \times \left( \frac{L}{W} \right).$$

In the case of 3D,  $\sigma_{3D} = \left( \frac{I_{SD}}{V_{SD}} \right) \times \left( \frac{L}{W} \right) \times \left( \frac{1}{t} \right)$ , where  $t$  is the thickness of nanosheets.

The resistivity ( $\rho$  in  $\Omega \text{ cm}$ ) is  $1/\sigma_{3D}$ . **Table S1** summarized the results of FET devices: carrier mobility  $\mu$  ( $\text{cm}^2 \text{V}^{-1} \text{s}^{-1}$ ), carrier concentration in 2D ( $n_{2D}$  in  $\text{cm}^{-2}$ ) and 3D ( $n_{3D}$  in  $\text{cm}^{-3}$ ), and resistivity ( $\Omega \text{ cm}$ ).

(b) The 2D carrier concentration ( $n_{2D}$ ) decreases with decreasing the thickness. The extrapolation (marked by the dotted line) indicates that  $n_{2D}$  of monolayer approaches to  $10^9 \text{ cm}^{-2}$ .

(c) The resistivity decreases with increasing the thickness. It approaches 0.06  $\Omega\cdot\text{cm}$  for the infinite thickness (bulk), which is close to 0.07  $\Omega\cdot\text{cm}$ , which was reported by Lee *et al.*<sup>S3</sup>

**Table S1.** Thickness-dependent characteristics of GeP nanosheets measured by FET devices. The experimental data has 10% uncertainty.

No.	$t$ (nm)	$L$ ( $\mu\text{m}$ )	$W$ ( $\mu\text{m}$ )	$V_{SD}$ (V)	$g_m$ ( $\text{A V}^{-1}$ )	$\mu$ ( $\text{cm}^2 \text{V}^{-1} \text{s}^{-1}$ )	<i>on/off</i>	$\left(\frac{I_{SD}}{V_{SD}}\right)$	$n_{2D}$ ( $\text{cm}^{-2}$ )	$n_{3D}$ ( $\text{cm}^{-3}$ )	$\rho$ ( $\Omega \text{cm}$ )
1	5.7	1.0	0.85	0.1	$2.93\times 10^{-11}$	0.030	$10^4$	$1.48\times 10^{-10}$	$3.62\times 10^{10}$	$6.45\times 10^{16}$	3262
2	7.2	1.4	1.0	0.1	$1.50\times 10^{-10}$	0.18	18	$6.16\times 10^{-9}$	$3.00\times 10^{11}$	$4.10\times 10^{17}$	55.5
3	7.8	0.5	0.6	0.05	$2.54\times 10^{-11}$	0.033	20	$8.70\times 10^{-9}$	$8.84\times 10^{12}$	$9.23\times 10^{16}$	116
4	10.6	0.25	1.3	0.1	$7.82\times 10^{-10}$	0.13	10	$6.75\times 10^{-8}$	$6.19\times 10^{11}$	$5.84\times 10^{17}$	82
5	11.0	0.8	0.3	0.01	$1.14\times 10^{-11}$	0.26	6	$3.72\times 10^{-10}$	$2.35\times 10^{12}$	$2.10\times 10^{17}$	16.8
6	11.6	0.25	0.1	0.1	$2.1\times 10^{-10}$	0.46	7	$8.81\times 10^{-8}$	$3.30\times 10^{12}$	$2.59\times 10^{18}$	5.43
7	13.1	0.8	2.6	0.05	$1.49\times 10^{-9}$	0.80	1.2	$7.55\times 10^{-6}$	$1.82\times 10^{13}$	$1.39\times 10^{19}$	0.56
8	15.6	1	0.3	0.1	$2.70\times 10^{-10}$	0.78	1.4	$5.77\times 10^{-7}$	$1.54\times 10^{13}$	$9.87\times 10^{18}$	0.81
9	21.2	2.8	1.7	3.0	$2.10\times 10^{-8}$	1.00	2	$2.64\times 10^{-7}$	$2.70\times 10^{13}$	$1.27\times 10^{19}$	0.40
10	24.4	0.80	1.0	0.01	$3.21\times 10^{-10}$	2.23	1	$1.36\times 10^{-5}$	$3.03\times 10^{13}$	$1.24\times 10^{19}$	0.23
11	31.2	0.84	0.27	0.1	$1.57\times 10^{-9}$	4.24	1	$7.76\times 10^{-6}$	$3.55\times 10^{13}$	$1.43\times 10^{19}$	0.13
12	76.2	1.75	3.57	0.1	$1.06\times 10^{-8}$	4.51	1	$2.58\times 10^{-5}$	$1.75\times 10^{14}$	$2.23\times 10^{19}$	0.062

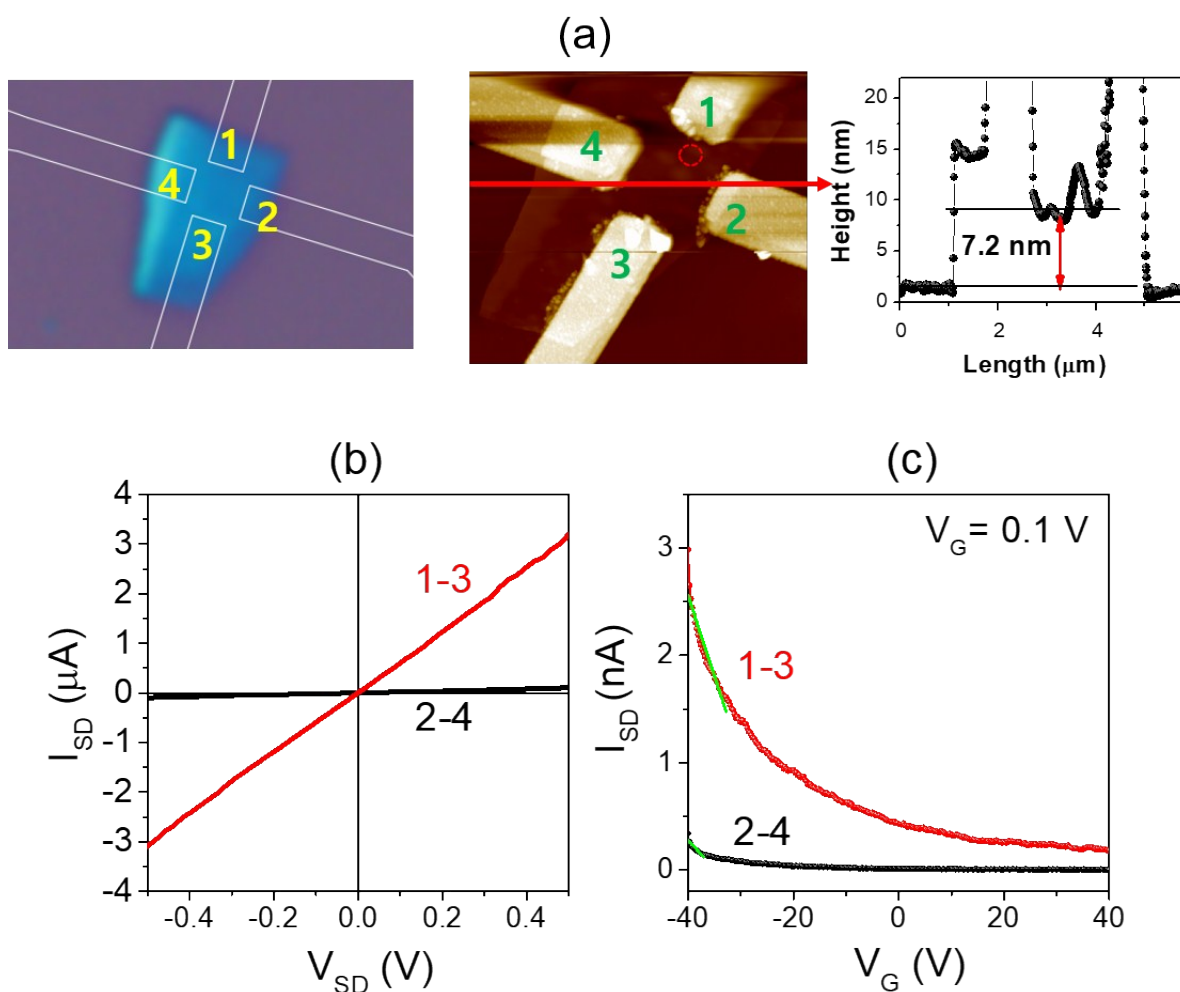


**Figure S6.** Anisotropic electrical properties of the rectangular shaped GeP nanosheets using FET devices. (a) Photograph/AFM images and high profiles shows a thickness of 7.2 nm. The length of long axis is about 5  $\mu\text{m}$ . (b) I–V curves ( $I_{\text{SD}}$  vs.  $V_{\text{SD}}$ ) of **1-3** and **2-4** electrodes whose distance is 1  $\mu\text{m}$ . (c) Source-drain current ( $I_{\text{SD}}$ ) vs. gate voltage ( $V_{\text{G}}$ ) curves of **1-3** and **2-4** electrodes.

The four electrodes are spaced at an angle of  $90^\circ$ , and **1-3** pair of diagonal electrodes is along the long axis while **2-4** pair of diagonal electrodes is perpendicular to it. The I–V curves of **1-3** electrode exhibits the higher carrier mobility and conductivity than those of **2-4** electrode. **Table S2** summarized the results of FET devices. The anisotropic factor of the electrical conductivity is 12, which is higher than the work (1.52) of Li et al.<sup>S2</sup> The anisotropic factor of carrier mobility is 2.4.

**Table S2.** Anisotropic electrical properties of GeP nanosheets measured by FET devices.

<i>No.</i>	<i>t</i> (nm)	<i>L</i> ( $\mu\text{m}$ )	<i>W</i> ( $\mu\text{m}$ )	$V_{\text{SD}}$ (V)	$g_m$ (A V <sup>-1</sup> )	$\mu$ (cm <sup>2</sup> V <sup>-1</sup> s <sup>-1</sup> )	<i>on/off</i>	$\left(\frac{I_{\text{SD}}}{V_{\text{SD}}}\right)$	$n_{2\text{D}}$ (cm <sup>-2</sup> )	$n_{3\text{D}}$ (cm <sup>-3</sup> )	$\rho$ ( $\Omega$ cm)
1-3	7.2	1.4	1.0	0.1	$1.50 \times 10^{-10}$	0.18	18	$6.16 \times 10^{-9}$	$3.00 \times 10^{11}$	$4.10 \times 10^{17}$	55.5
2-4	7.2	1.4	1.0	0.1	$6.27 \times 10^{-11}$	0.075	297	$1.91 \times 10^{-10}$	$2.53 \times 10^{10}$	$3.47 \times 10^{16}$	656

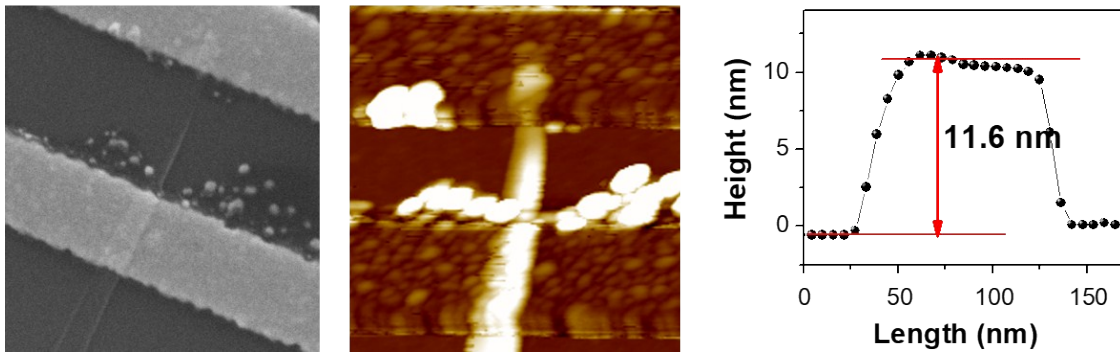
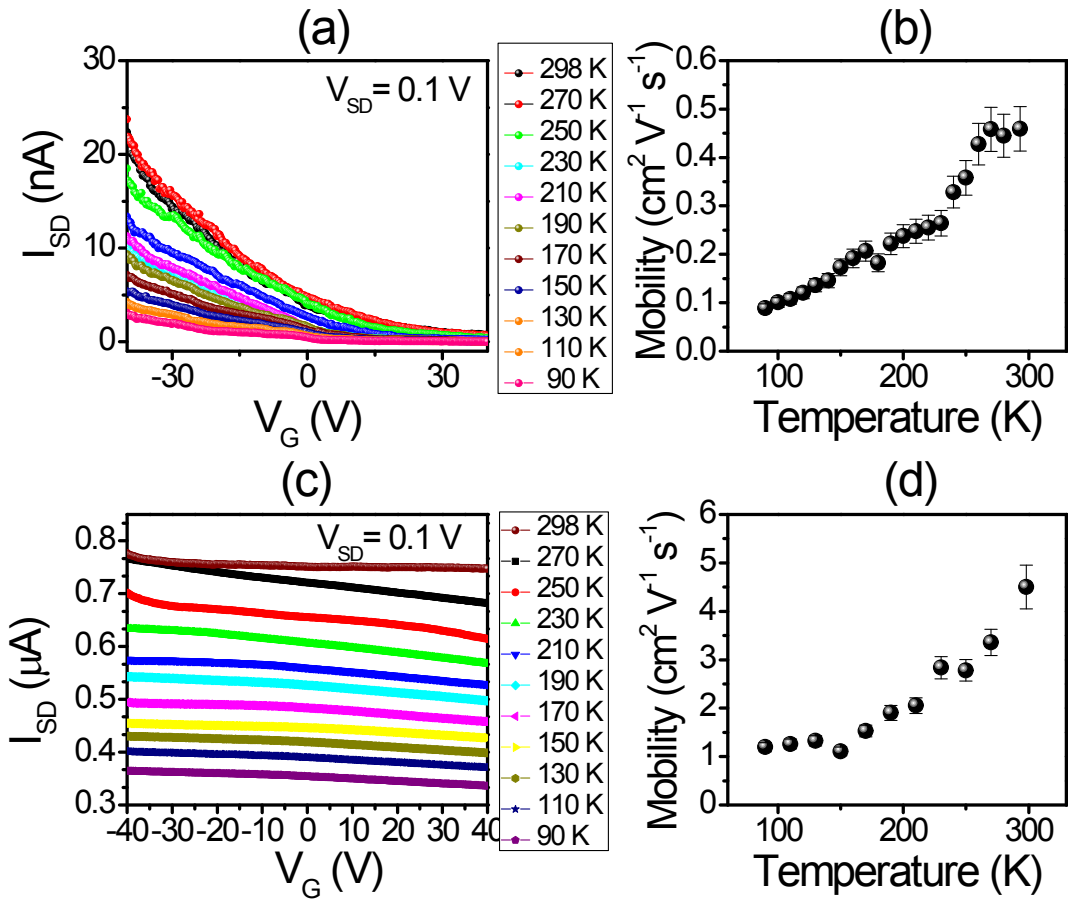


**Figure S7.** Temperature-dependent gate effect of FET devices and carrier mobility of GeP nanosheets with a thickness of (a), (b) 11.6 nm and (c), (d) 31.2 nm. The AFM images and height profile for 11.6 nm electrode is shown in the bottom. The AFM data for 31.2 nm are shown in **Figure S5**.

Carrier mobility shows a strong dependence on operation temperature. For both 11.6 nm and 31.2 nm thick GeP nanosheets, a decrease in the mobility is observed as the temperature is lowered to 90 K, showing good agreement with the carrier mobility limited by charged-

impurity scattering, which depends on the speeds of carriers and the concentration of the ionized impurity. This is because when temperature increases, the average thermal speeds of the carriers are also increased. Hence, the carriers spend less time near the ionized impurity and thus the scattering effect of the ions is reduced, which concomitantly leads to higher mobility. It suggests that the charged-impurity scattering is a major important factor in determining the mobility of GeP nanosheets.

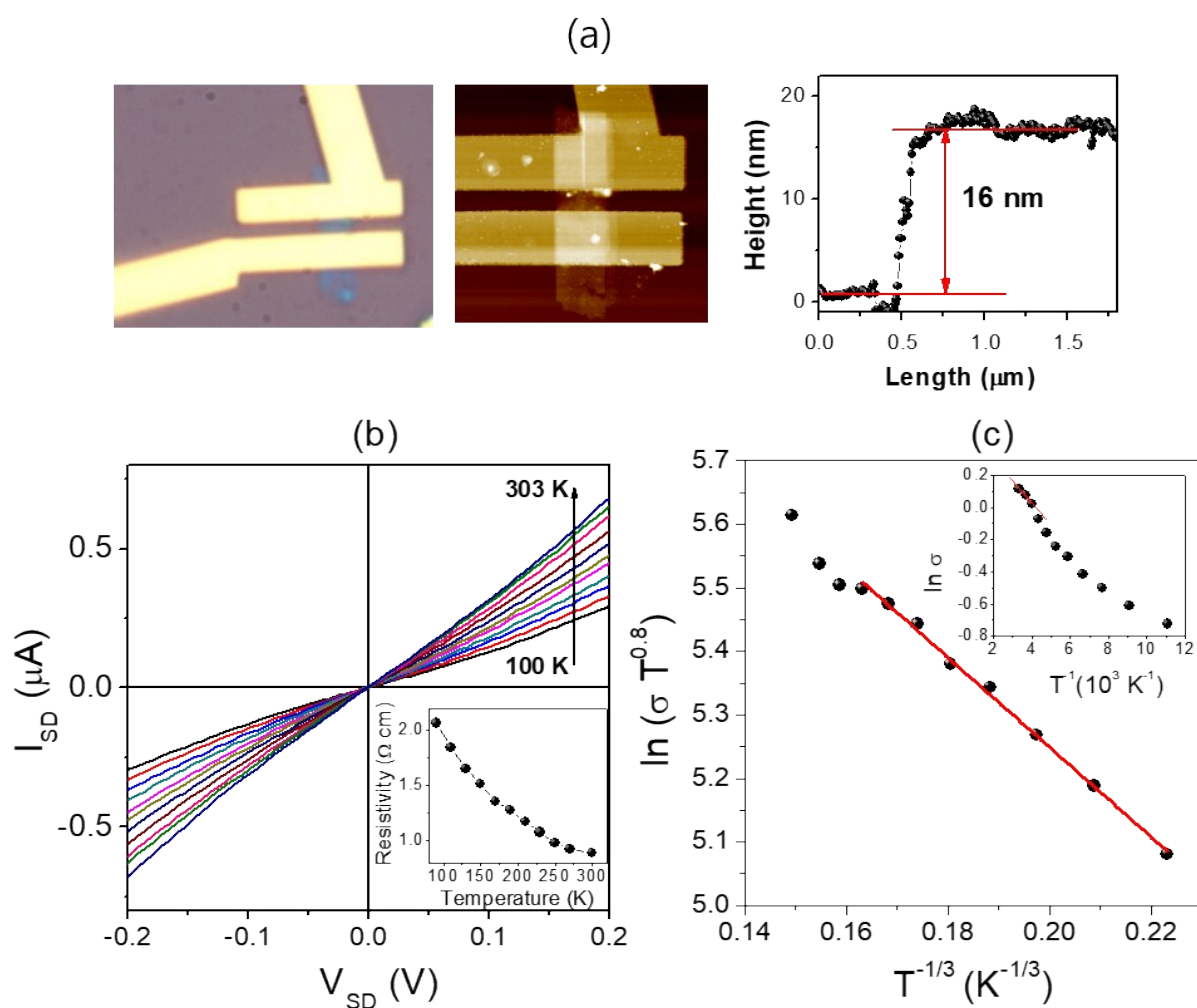


**Figure S8.** (a) Photograph, and AFM image and height profile showing that the thickness of GeP nanosheet is 16 nm. (b) I–V curves of the GeP electrode as a function of temperature. (c)  $\ln(\text{conductivity } T^{0.8})$  vs.  $T^{-1/3}$  and  $\ln(\text{conductivity})$  vs.  $1/T$  (inset) plots.

(a) The AFM image and the height profile (scanned from the left to the right) show that the GeP nanosheet has a thickness of 16 nm. The channel length is 1  $\mu\text{m}$  and the width is 1.9  $\mu\text{m}$ .

(b) The current–voltage ( $I_{\text{SD}}-V_{\text{SD}}$ ) characteristics were measured as a function of temperature (100–300 K). The two-terminal  $I_{\text{SD}}-V_{\text{SD}}$  curves exhibit a nearly linear response, and thus the contacts behave as ohmic ones. The current increases with increasing temperature, which is typical for semiconductors due to thermally activated conduction.

(c) The conductivity ( $\sigma$  in  $\text{S}\cdot\text{cm}^{-1}$ ) in the high-temperature regime (250–300 K) was measured and used to obtain an Arrhenius plot ( $\ln \sigma$  versus  $T^{-1}$ ). The obtained thermal activation energy

( $E_a = 10$  meV) is close to the thermal energy (26 meV) at this temperature range (inset). It indicates that the conductivity is determined by the thermal activation of the GeP channel. However, the conductivity in the low-temperature regime (100-250 K) deviates from the thermal conduction behavior. The  $\ln(\sigma \cdot T^{0.8})$  versus  $T^{-1/3}$  plot with a linear fit. Therefore, the temperature-dependent conductivity is well described by the Variable-Range-Hopping (VRH) mechanism that is expressed by 2D Mott's law:  $\sigma = \sigma_0(T) \exp[-(T_0/T)]^{1/3}$ , where  $T_0$  is correlation energy scale and  $\sigma_0 = AT^m$  with  $m = 0.8-1$ .<sup>S4</sup> The characteristic temperature dependence is a signature of hopping transport via localized states. The electrical conductivity of GeP follows the typical behavior of 2D materials. Because Mott's VRH is related to multiple localized states along the 2D channel, defect sites induced by moderately *p*-type doped Ge vacancies could act as the multiple states.

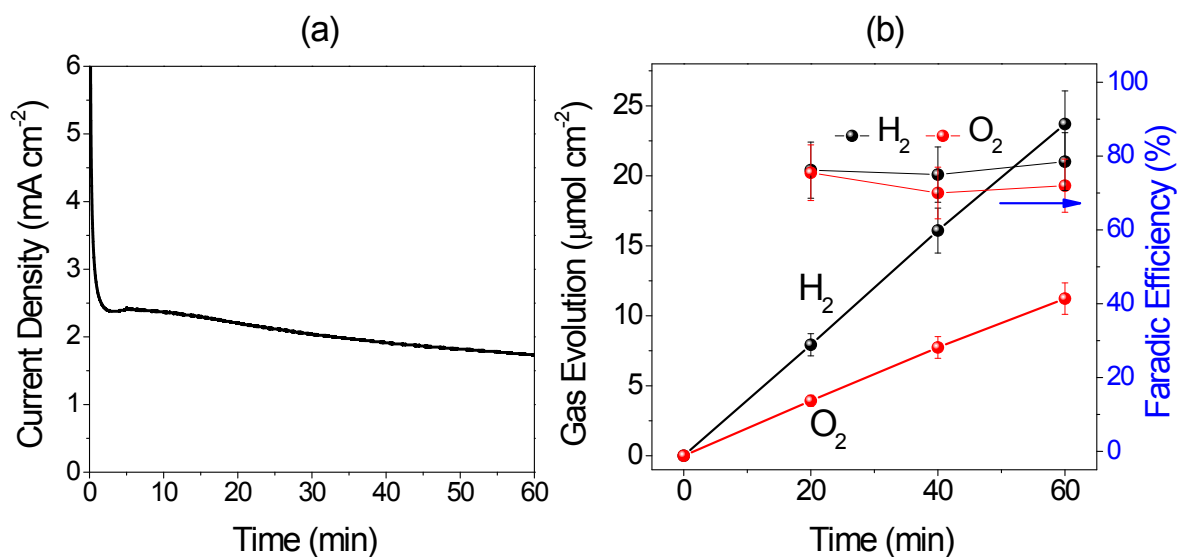


**Figure S9.** (a) Stability of photocurrent and (b) H<sub>2</sub> and O<sub>2</sub> evolution under the applied potential of 1 V vs. RHE.

The photocurrent decreased significantly for first 2 min. The decrease could be explained by the reduced concentration of the active sites due to the surface oxidation of Si NWs (mainly), which cannot be avoidable. The less decrease after 2 min is probably due to the maintain the GeP and Si phases underneath the oxide layers. The 2:1 stoichiometric ratio of H<sub>2</sub>:O<sub>2</sub> confirmed the photocatalytic water-splitting reaction: 2H<sub>2</sub>O (l) → O<sub>2</sub> (g) + 4H<sup>+</sup> + 4e<sup>-</sup> at the anode, and 2H<sup>+</sup> + 2e<sup>-</sup> → H<sub>2</sub> (g) at the cathode. Faradic efficiency (*FE*) for the production of H<sub>2</sub> and O<sub>2</sub> was

calculated by  $FE_{H_2} = \frac{2 \times N_{H_2} \times 96485}{Q}$  and  $FE_{O_2} = \frac{4 \times N_{O_2} \times 96485}{Q}$ , where  $N_{H_2}$  and  $N_{O_2}$  are the amounts (mol) of H<sub>2</sub> and O<sub>2</sub>, respectively, and  $Q$  is the total amount of generated charge in coulomb (photocurrent × time). The obtained Faradic efficiency was about 75%.

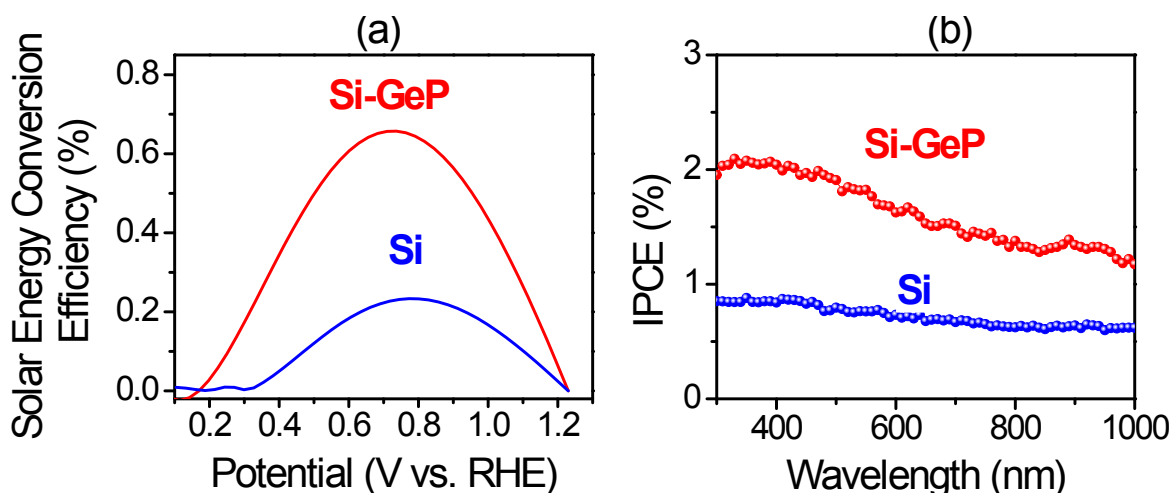


**Figure S10.** (a) Solar energy conversion efficiency of the photoanodes (Si and Si-GeP) calculated from the photocurrent-potential curves. See **Table S3** for the parameters of PEC cells. (b) Measured IPCE spectrum, collected at the incident wavelength range from 300-1000 nm, at potential of 1.23 V vs. RHE.

(a) The solar energy conversion efficiency ( $\eta$ ) is plotted as a function of applied potential, using the current–potential curves shown in Fig. 5d. The  $\eta$  value as a function of the applied

potential was calculated using the following equation: 
$$\eta = \frac{J_{SC} |V_{OC} - E^0| FF}{I_{ph}}$$
, where  $J_{SC}$  is the short-circuit current corresponding to the current density at the water oxidation potential (1.23 V vs. RHE),  $V_{OC}$  is open-circuit voltage (onset potential),  $E^0$  is the water oxidation potential (= 1.23 V),  $FF$  is the fill factor determined using the photocurrent density at each applied potential, and  $I_{ph}$  is the incident photon density (= 100 mW cm<sup>-2</sup> in this work). The maximum  $\eta$  value is 0.65%. The corresponding solar-to-hydrogen conversion efficiency is 0.65% × 0.75 = 0.49%. The cell parameters are summarized in **Table S3**.

**Table S3.** PEC cell parameters for maximum solar energy conversion efficiency ( $\eta$ ) and solar-to-hydrogen conversion efficiency ( $\eta_{H_2}$ ).

	$V_{OC}$ (V)	$J_{SC}$ (mA cm <sup>-2</sup> )	$E$ (V) <sup>a</sup>	$J$ (mA cm <sup>-2</sup> ) <sup>a</sup>	FF	$\eta$ (%)	$\eta_{H_2}$ (%)
Si	0.35	0.8	0.77	0.51	0.33	0.23	--
Si-GeP	0.25	2.3	0.72	1.8	0.44	0.65	0.49

<sup>a</sup> Voltage (vs. RHE) and current density at maximum conversion efficiency ( $\eta$ ).

(b) We performed incident-photon-to-current-conversion efficiency (IPCE) measurements to study their photoresponse as a function of incident light wavelength. The IPCE at different wavelengths is determined from the short circuit photocurrents ( $I_{sc}$ ) monitored at different excitation wavelengths ( $\lambda$ ) to compare the photoresponse of the samples using an equation,  $IPCE (\%) = [1240 \times I_{sc} (\text{mA}/\text{cm}^2)] / [\lambda(\text{nm})/I_{ph} (\text{W}/\text{cm}^2)] \times 100$ , where  $I_{ph}$  is the incident light power. The Si and Si-GeP has the IPCE over the entire visible light wavelength range, which is in good agreement with the band gap of Si (1.18 eV). A maximum IPCE of 2 % is achieved for the Si-GeP electrode. Under the same conditions, the maximum IPCE value of 0.9 % for Si is observed. In addition, because the light absorption of photoanodes is major from the n-Si due to the ultrathin GeP nanosheets, the Si and Si-GeP photoanodes present a similar spectral response. But it is worth noting that the IPCE value for the Si-GeP photoanode exhibits an enhancement in the range of 300–600 nm, which corresponds to the absorption band induced by GeP nanosheets.

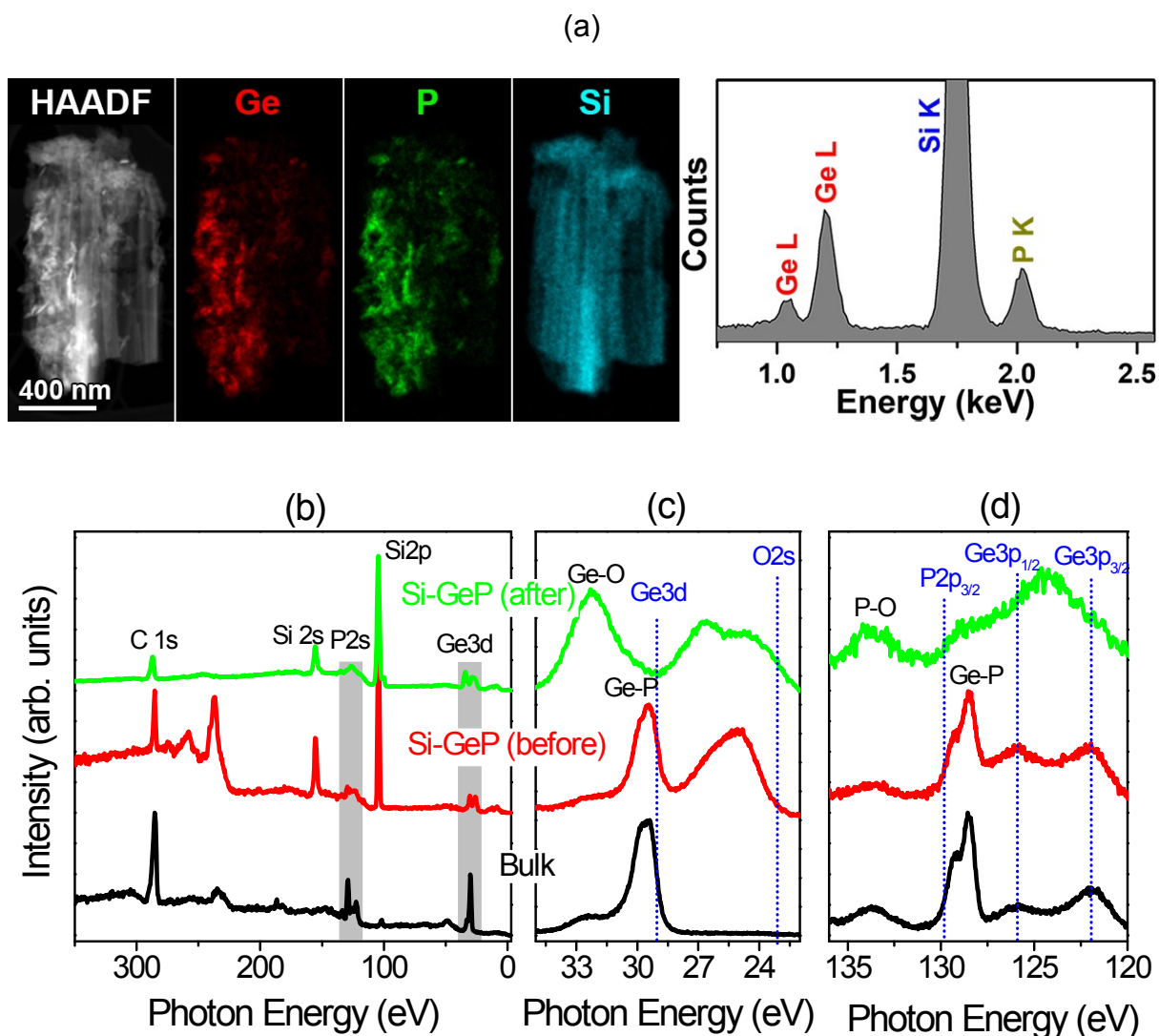


**Figure S11.** (a) HAADF STEM image of the Si-GeP core-shell NW after 1 h PEC water splitting reaction, and EDX mapping of Ge L-shell, P K-shell, and Si K-shell, and the corresponding EDX spectra. (b) XPS survey scans of the bulk GeP and Si-GeP before/after 1 h PEC water splitting reaction. Fine-scanned XPS (c) Ge 3d and (d) P 2p and Ge 3p peaks. The peak position of neutral state is marked by the blue lines.

(a) HAADF STEM image, the EDX elemental mapping (Ge L-shell, P K-shell, and Si K-shell), and the corresponding EDX spectra for the Si-GeP photoanodes after 1 h PEC water splitting reaction. The Ge and P atoms exist in the nanosheets (at the shell part) and Si only exists in the

NWs (at the core part).

(b) XPS survey scans of the bulk GeP and Si-GeP before/after 1 h PEC water splitting reaction. show the Si peak in the Si-GeP samples.

(c) The Ge 3d peak and O1s appear in 22-35 eV region. The neutral Ge ( $\text{Ge}^0$ ) should appear at 29.4 eV. The bulk GeP powders and Si-GeP before samples show the Ge-P bonding peak at 29.6 eV, which is blue shifted from the neutral position. However, the Si-GeP after samples show the peak at 32.4 eV, corresponding to Ge-O peak. The Si-GeP sample shows the O 2s peaks at 25 and 26.5 eV, which is blue-shifted from the neutral O at 23 eV. These peaks are assigned to the O-H/S-O/N-O bonding structures that generated from the exfoliation in NMP as well as the electrolyte ( $\text{Na}_2\text{SO}_4/\text{NaOH}$ ).

(c) The bulk GeP powders and Si-GeP show the P  $2p_{3/2}$  and P  $2p_{1/2}$  peaks of Ge-P bonding structures at 128.4 and 129.2 eV, which are about 1.5 eV red-shifted with respect to the signal of neutral P ( $\text{P}^0$ ) at 129.9 and 129.1 eV (separated by 0.8 eV), respectively. The peak at 133.8 eV correspond to that of the oxide P-O. The Ge  $3p_{3/2}$  and Ge  $3p_{1/2}$  peaks of Ge-P bonding structures appear at 122 and 126 eV, which is close to those of neutral Ge ( $\text{Ge}^0$ ) at 122 and 126 eV, respectively. After PEC, the intensity of P-O peak increases. Furthermore, the Ge  $3p_{3/2}$  and Ge  $3p_{1/2}$  peaks are blue shifted to 125 eV and 129 eV. Therefore, the Si-GeP underwent the surface oxidation during the PEC water splitting reaction.

**Table S4.** Comparison of PEC performance (in pH 0) of Si photoanode in the literatures; onset potential (vs. RHE), current density at 1.23 V ( $J_{1.23V}$ ), maximum applied bias photon-to-current (ABPC) or photon-to-H<sub>2</sub> (or O<sub>2</sub>), and faradic efficiency for H<sub>2</sub> evolution ( $\eta_{H_2}$ ).

No.	Materials (electrolyte)	Onset potential (V) vs. RHE	$J_{1.23V}$ (mA cm <sup>-2</sup> )	ABPC (%)	$\eta_{H_2}$ (%)
S5	CoOx/Si (1M NaOH)	1.03	30.8	--	--
S6	Ni/Si (1M NaOH)	0.95	30	3.39	--
S7	Ni/TiO <sub>2</sub> /Si (1M KOH)	1.03	35	0.779	--
S8	MoSe <sub>2</sub> /p+-n Si (1M HBr)	0.3	30	14	--
S9	Ni-O/Ni/Si (1M NaOH)	0.93	39.7	3.2	90
S10	NiFe@Si (1M NaOH)	1.05	32	1.2	--
S11	Ni-Mo/Ni/n <sup>++</sup> -Si (1M KOH)	0.95	35	3.2	--
S12	n-Si/CoOx/NiCuOx (1M NaOH)	1.0	35	1.4	--
Present work	n-Si@GeP (0.1 M Na <sub>2</sub> SO <sub>4</sub> /0.25 M NaOH)	0.25	2.3	0.65	75

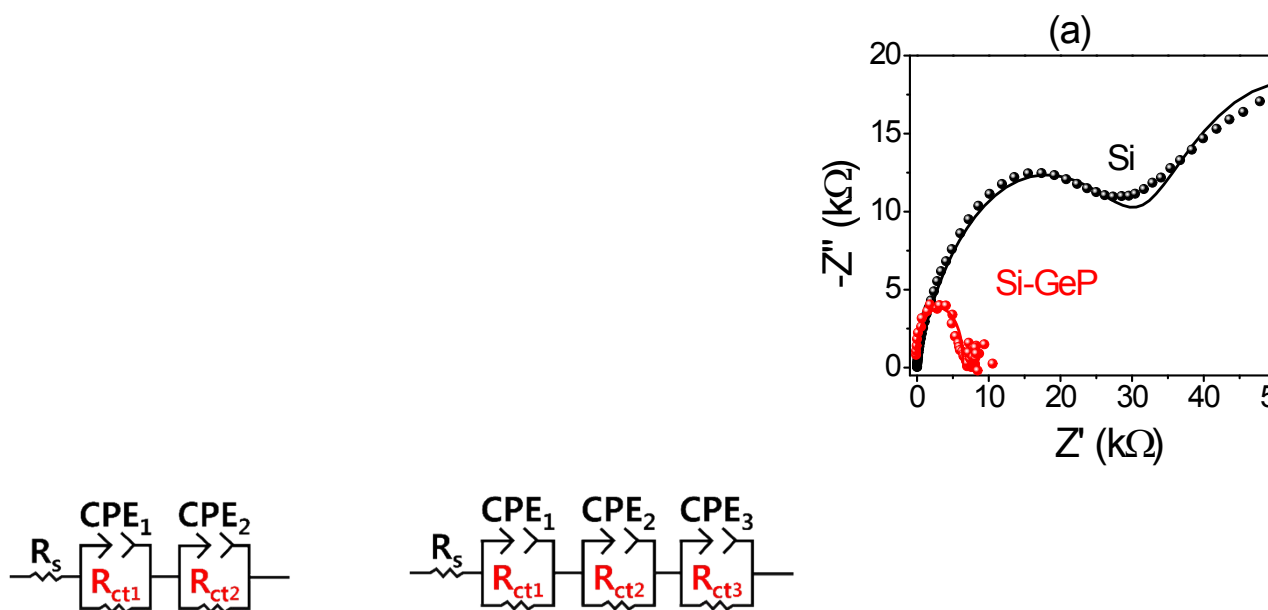


**Figure S12.** Nyquist plots of Si NW and Si-GeP NWs for electrochemical impedance spectroscopy (EIS) experiments in the range from 1 MHz to 0.1 Hz at 0 V (vs. RHE) in a 0.1 M Na<sub>2</sub>SO<sub>4</sub>/0.25 M NaOH electrolyte, under (a) dark and (b) the irradiation of AM1.5G 100 mW cm<sup>-2</sup> using Xe lamp. The equivalent circuits are shown and the fitting curves are represented by the solid lines.

**Table S5.** Impedance fitting parameter  $R_e$  represents the internal resistance of the electrolyte,  $R_{ct}$  is associated with the charge transfer resistance between the electrode and electrolyte, and CPE represents the constant-phase element related to the double-layer capacitance.

(a) In dark							
	$R_s$ ( $\Omega$ )	$R_{ct1}$ (k $\Omega$ )	$CPE_1 \times 10^{-5}$	$R_{ct1}$ (k $\Omega$ )	$CPE_2 \times 10^{-5}$		
Si	1.0	33.3	7.5	46.0	1.2		
Si-GeP	1.0	7.3	2.1	1.6	1.7		
(b) Under light irradiation							
	$R_s$ ( $\Omega$ )	$R_{ct1}$ (k $\Omega$ )	$CPE_1 \times 10^{-5}$	$R_{ct2}$ (k $\Omega$ )	$CPE_2 \times 10^{-5}$	$R_{ct3}$ (k $\Omega$ )	$CPE_3 \times 10^{-5}$
Si	1.0	3.9	1.9	5.3	1.9	-	-

Si-GeP	1.0	0.8	2.7	0.79	3.2	1.4	9.9
--------	-----	-----	-----	------	-----	-----	-----

EIS measurements in a 0.1 M Na<sub>2</sub>SO<sub>4</sub>/0.25 M NaOH electrolyte were carried out for the electrode by applying an AC voltage of 20 mV at a bias voltage of 1.23 V (vs. RHE). The *x*- and *y*-axes are the real part (*Z'*) and negative imaginary part (*-Z''*) of the impedance, respectively. A semicircle in the Nyquist plot at high frequencies represents the charge transfer process, with the diameter of the semicircle reflecting the charge-transfer resistance. The simulation of EIS spectra (fitted lines) using an equivalent circuit model yielded the *R*<sub>ct</sub> values. The fitting parameter *R*<sub>e</sub> represents the internal resistance of the electrolyte, and CPE represents the constant-phase element related to the double-layer capacitance.

The simulation of EIS spectra (fitted line) using an equivalent circuit model (inset) yielded the two *R*<sub>ct</sub> (*R*<sub>ct1</sub> and *R*<sub>ct2</sub>) or three (*R*<sub>ct1</sub>, *R*<sub>ct2</sub>, and *R*<sub>ct3</sub>) values, with corresponding CPE. In the dark, two semicircles appear at high frequency range. The sum of *R*<sub>ct1</sub> and *R*<sub>ct2</sub> is 79.3 kΩ for Si and 8.9 kΩ for Si-GeP. Under light irradiation, the sum of *R*<sub>ct1</sub> and *R*<sub>ct2</sub> is 9.2 kΩ for Si. In the case of Si-GeP, the fitting of three semicircles at high frequency range provides the sum of *R*<sub>ct1</sub>, *R*<sub>ct2</sub>, and *R*<sub>ct3</sub> as 2.99 kΩ. The large *R*<sub>ct</sub> value of Si NWs confirmed the sluggish charge transfer kinetics on the surface of Si. The smaller *R*<sub>ct</sub> value of *n*-Si/*p*-GeP indicates the much efficient charge transfer of photoelectrode and electrolyte interface.

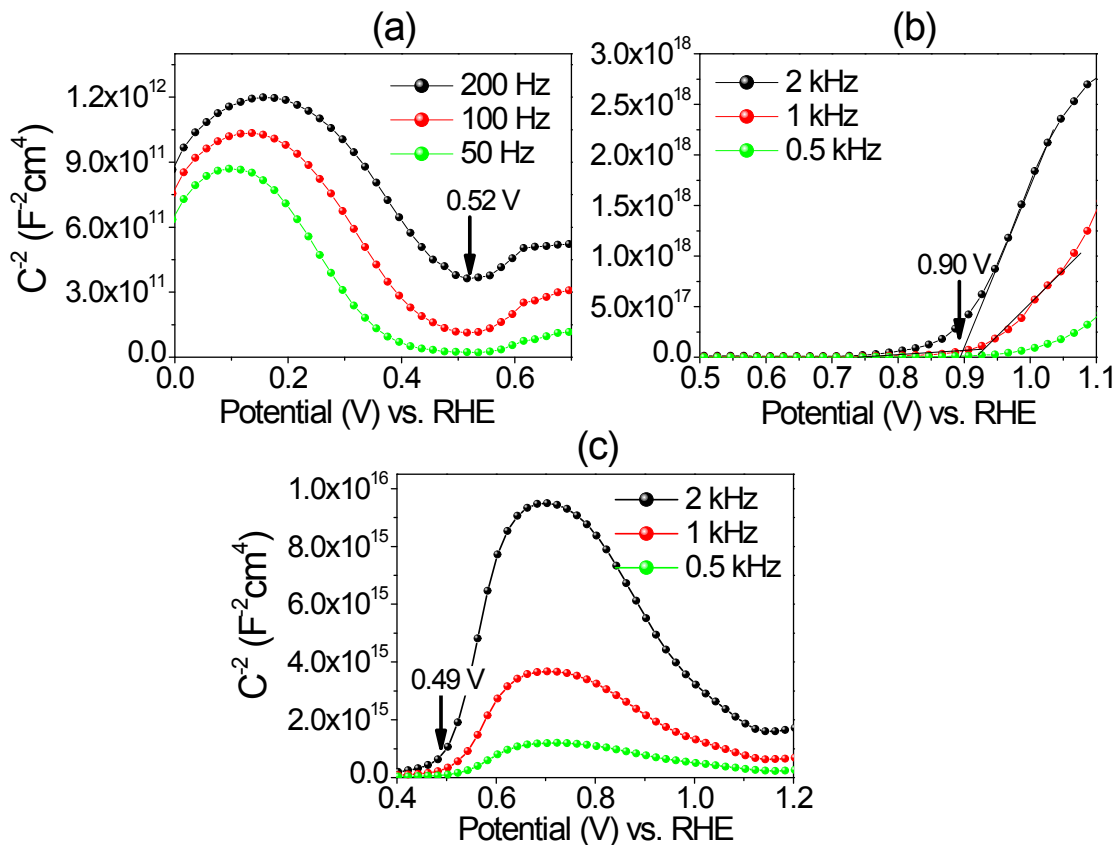


**Figure S13.** Mott–Schottky (MS) plots for the (a) GeP nanosheets (on GC electrode) at 50, 100, and 200 Hz in a 0.1 M  $\text{Na}_2\text{SO}_4/0.25$  M NaOH electrolyte. MS plots for (b) Si NWs and (c) Si-GeP NWs at 0.5, 1, and 2 kHz. The flat band potentials are obtained from the intercepts of the extrapolated lines.

The flat band potentials ( $E_{\text{fb}}$ ) were investigated using Mott–Schottky (MS) plots, *i.e.*, the reciprocal of capacitance vs. the applied potential. These MS plots were measured by anodically sweeping the potential with an AC amplitude of 10 mV. For GeP nanosheets, the linear plots with negative slope confirm the *p*-type character. The lines show the linear regions of the MS plots, and the  $E_{\text{fb}}$  value is obtained from the intercepts of the extrapolated lines. The  $E_{\text{fb}}$  value of GeP was determined to be 0.52 V vs. RHE. For Si NWs and Si-GeP NWs, the positive slope is due to the *n*-type character of Si NWs. The  $E_{\text{fb}}$  values of Si NWs and Si-GeP NWs were determined as 0.90 and 0.49 V (vs. RHE), respectively. The  $E_{\text{fb}}$  position of Si-GeP is negatively shifted by about 0.41 V relative to that of Si. The negative shift is consistent with the cathodic shift of the onset potentials in the PEC cell. Therefore, the cathodic shift of the onset potential of PEC cell upon the GeP deposition is attributed to that of the  $E_{\text{fb}}$  position. The discrepancy between the  $E_{\text{fb}}$  and the photocurrent onset is likely due to the overpotential losses and voltage drop in the circuit.

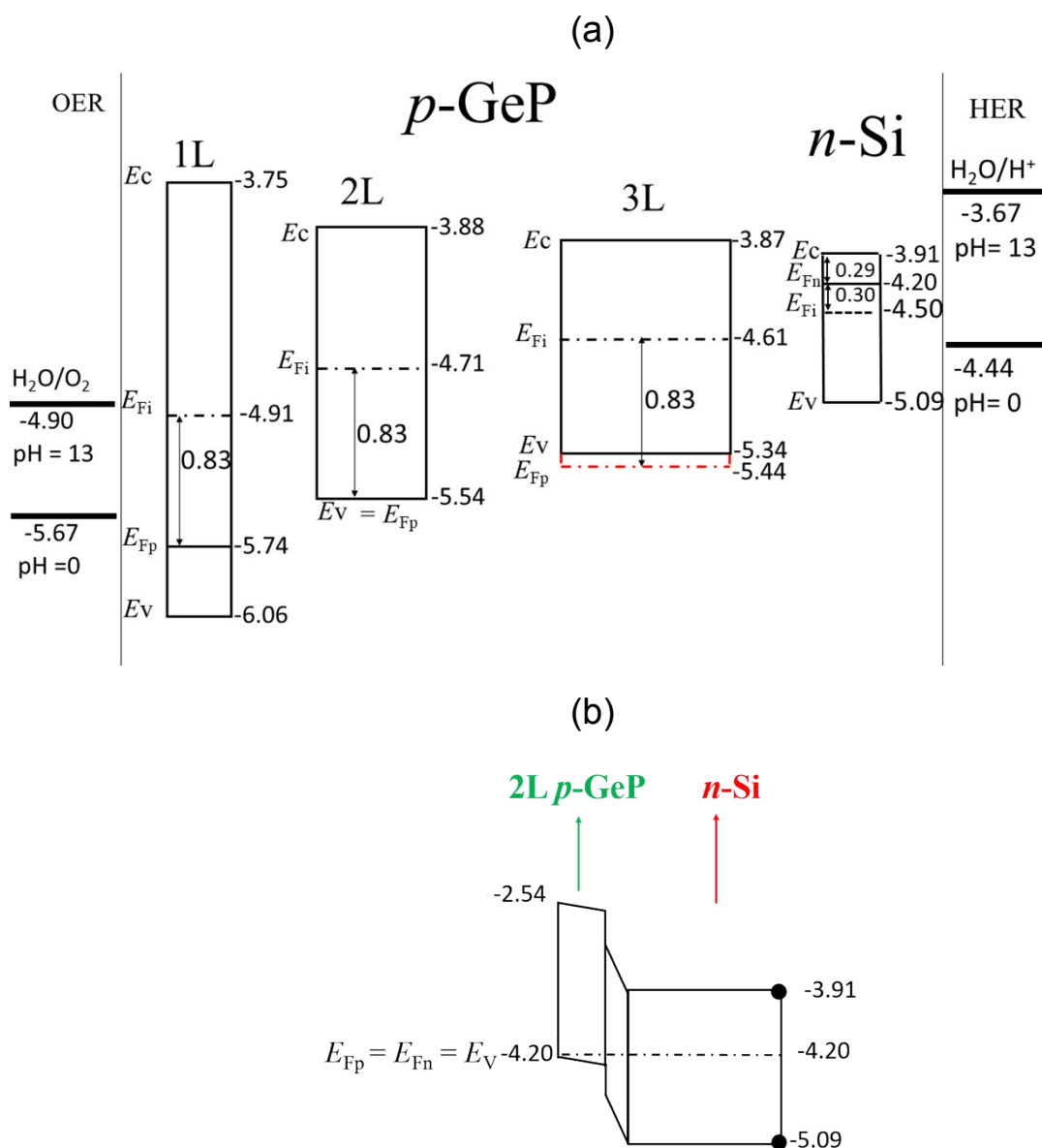


**Figure S14.** (a) Band diagram of  $p$ -GeP (1L, 2L, and 3L) and  $n$ -Si (in vacuum) before contact which are drawn based on our calculation. The positions of the CBM ( $E_C$ ), VBM ( $E_V$ ), and Fermi level ( $E_{Fi}$ ,  $E_{Fp}$ , and  $E_{Fn}$ ) versus vacuum level are shown together with the Fermi levels of the HER and OER at pH 0 and 13 (right and left ends). (b) Band diagram of the GeP (2L) and  $n$ -Si in contact.

The intrinsic 2D hole concentration (per unit area)  $p_i^{(2)}$  of GeP 1L was calculated as  $2.28 \times 10^{-5} \text{ cm}^{-2}$  using the electronic densities of states and the Fermi-Dirac occupation. The experiments showed that the hole concentration significantly decreases as the layer number decreases (see **Figure S5**). We estimated  $p_0^{(2)} = 2 \times 10^9 \text{ cm}^{-2}$  for the GeP 2L by extrapolating

the thickness-dependent hole concentration (since  $p_0^{(2)} = 10^9 \text{ cm}^{-2}$  for 1L, as shown in **Figure S5**). Therefore, the GeP 2L could be heavily doped in such a way that the Fermi level ( $E_{\text{Fp}}$ ) is located at 0.83 eV below its intrinsic level ( $E_{\text{Fi}}$ ), using the formula,  $E_{\text{Fp}} - E_{\text{Fi}} = kT \ln(p_0/p_i) = 0.026 \ln\left(\frac{2 \times 10^9}{22.28 \times 10^{-5}}\right) = 0.83 \text{ V}$ . So the Fermi level of GeP 2L is located close to its VBM (-5.54 eV).

Si has an intrinsic band gap of 1.18 eV and its calculated electron concentration ( $n_i$ ) is  $1.5 \times 10^{10} \text{ cm}^{-3}$ . The intrinsic Fermi level ( $E_{\text{Fi}}$ ), VBM, and CBM are located at -4.50, -5.09, and -3.91 eV, respectively. Since  $n$ -Si NWs were fabricated using the phosphorous-doped Si wafer having  $R = 1\text{--}10 \ \Omega \text{ cm}$ , we calculated the electron concentration ( $n_0$ ) of  $n$ -Si to be in the range of  $3.0 \times 10^{14}\text{--}5.0 \times 10^{15} \text{ cm}^{-3}$ . We assumed  $n_0 = 1.5 \times 10^{15} \text{ cm}^{-3}$  for  $n$ -Si by taking the center value. The Fermi level ( $E_{\text{Fn}}$ ) was shifted upward to -4.20 eV, following the relation  $E_{\text{Fn}} - E_{\text{Fi}} = kT \ln$

$$\left(\frac{n_0/n_i}{n_0/n_i}\right) = 0.026 \ln\left(\frac{1.5 \times 10^{15}}{1.5 \times 10^{10}}\right) = 0.30 \text{ eV. The } E_{\text{Fn}} \text{ lies } 0.29 \text{ eV below the CBM level.}$$

Now we estimate the dimension of each side of the  $p$ - $n$  junction corresponding to the SCR for the  $p$ -GeP (2L) nanosheets and  $n$ -Si NW. The average radius and length of the Si NW are 100 nm and 6  $\mu\text{m}$ , respectively, so its volume is  $V_{(\text{Si NW})} = \pi \times (100 \text{ nm})^2 \times 6 \ \mu\text{m} = 1.8 \times 10^{-13} \text{ cm}^3$ . The number of electrons ( $N_0$ ) in each  $n$ -Si NW is  $(1.5 \times 10^{15} \text{ cm}^{-3}) \times (1.8 \times 10^{-13} \text{ cm}^3) = 2.7 \times 10^2$ . If the GeP nanosheets fully cover the surface of each  $n$ -Si NW, the number ( $P_0$ ) of holes in the corresponding GeP 2L nanosheet is  $P_{0(\text{GeP})} = (2 \times 10^9 \text{ cm}^{-2}) \times 2\pi \times (100 \text{ nm}) \times 6 \ \mu\text{m} = 76$ . Therefore, the ratio of carrier numbers is  $N_{0(n\text{-Si})}/P_{0(\text{GeP})} = (2.7 \times 10^2)/76 = 35$ , indicating that the number of electrons in the Si NW is much larger than the number of holes in the GeP nanosheets. Therefore, the Fermi level of the  $p$ - $n$  junction,  $E_{\text{F}(\text{GeP/Si})}$ , is the same as  $E_{\text{F}(\text{Si})}$ . The charge neutrality condition requires that the GeP is completely depleted, but only thin interface of  $n$ -Si in contact with the GeP will correspond to the SCR. The whole region of the Si support will remain intact. The built-in potential is  $eV_{\text{bi}} = |E_{\text{F}(\text{GeP})} - E_{\text{F}(\text{Si})}| = 1.34 \text{ V}$ , where  $E_{\text{F}(\text{GeP})} = -4.71 - 0.83 = -5.54 \text{ V}$  and  $E_{\text{F}(\text{Si})} = -4.20 \text{ V}$ . The potential drop in the  $n$ -Si region will be larger than that in the  $p$  region, which is reasonable from the estimation:  $V_{\text{bi},n}/V_{\text{bi},p} = \epsilon_{(\text{GeP})}P_{0(\text{GeP})}/\epsilon_{(\text{Si})}N_{0(\text{Si})} = 30 \epsilon_{(\text{GeP})}/\epsilon_{(\text{Si})} > 1$ . Although the charge screening is less effective in the 2D GeP than in the 3D Si, we do not expect that the ratio of the dielectric constants ( $\epsilon$ ) of the

two materials to be smaller than  $1/30$ .

## References

- S1. T. Wadsten, *Acta Chem. Scand.*, 1967, **21**, 593-594.
- S2. L. Li, W. Wang, P. Gong, X. Zhu, B. Deng, X. Shi, G. Gao, H. Li and T. Zhai, *Adv. Mater.*, **2018**, 1706771.
- S3. K. Lee, S. Synnestvedt, M. Bellard and K. Kovnir, *J. Solid State Chem.*, 2015, **224**, 62-70.
- S4. F. W. Van Keuls, X. L. Hu, H. W. Jiang and A. J. Dahm, *Phys. Rev. B*, 1997, **56**, 1161–1169.
- S5. J. Yang, J. K. Cooper, F. M. Toma, K. A. Walczak, M. Favaro, J. W. Beeman, L. H. Hess, C. Wang, C. Zhu, S. Gul, J. Yano, C. Kisielowski, A. Schwartzberg and I. D. Sharp, *Nat. Mater.* 2017, **16**, 335-341.
- S6. S. Oh, H. Song, and J. Oh, *Nano Lett.*, 2017, **17**, 5416-5422.
- S7. W. Hong, Q. Cai, R. Ban, X. He, C. Jian, J. Li, J. Li and W. Liu, *ACS Appl. Mater. Interfaces*, 2018, **10**, 6262-6268.
- S8. S. Vanka, Y. Wang, P. Ghamari, S. Chu, A. Pandey, P. Bhattacharya, I. Shih and Z. Mi, *Sol. RRL*, 2018, **2**, 1800113.
- S9. G. Huang, R. Fan, X. Zhou, Z. Xu, W. Zhou, W. Dong and M. Shen, *Chem. Commun.*, 2019, **55**, 377-380.
- S10. C. Li, M. Huang, Y. Zhong, L. Zhang, Y. Xiao and H. Zhu, *Chem. Mater.*, 2019, **31**, 171-178.
- S11. R. Fan, S. Cheng, G. Huang, Y. Wang, Y. Zhang, S. Vanka, G. A. Botton, Z. Mi and M. Shen, *J. Mater. Chem. A*, 2019, **7**, 2200-2209.
- S12. L. He, W. Zhou, L. Hong, D. Wei, G. Wang, X. Shi and S. Shen, *J. Phys. Chem. Lett.*, 2019, **10**, 2278-2285.
- S13. D. A. Neamen, “*Semiconductor Physics and Devices*,” 4<sup>th</sup> Ed., McGraw-Hill Korea, 2012, Chap. 4.